A Coded Aperture for High-Resolution Nuclear Medicine Planar Imaging With a Conventional Anger Camera: Experimental Results

Roberto Accorsi, Francesca Gasparini, and Richard C. Lanza, *Member, IEEE*

***Abstract*—As compared to pinholes and collimators, coded aperture cameras present the potential advantage of increased signal-to-noise ratio (SNR). This advantage can be used to improve the resolution of conventional imagers while still producing clear images. In this paper, we describe a near-field coded aperture camera with a field of view of 9 × 9 cm and 1.7-mm system resolution based on the use of an existing gamma-camera. Experimental results include planar *in-vivo* studies of ^{99m}Tc-labeled compounds in a mouse.**

***Index Terms*—Coded aperture imaging, high resolution, molecular imaging, nuclear medicine imaging, small animal imaging.**

I. Introduction

CODED apertures are an alternative way of producing images of radiating objects that has already been applied in the past, mainly in astronomy and space applications [1]–[3], but also in physics [4], [5] and nuclear medicine [6]–[8]. Coded apertures were initially developed as a way of improving the signal-to-noise ratio (SNR) of pinhole and collimator systems. All other factors being equal, a higher SNR means less noise in the images, but the SNR advantage can be traded off to reduce exposure times, improve resolution or, where applicable, reduce dose, while maintaining the same image quality.

Several families of coded aperture patterns, all having ideal imaging properties, are found in literature [9]–[15]. By "ideal imaging" we mean that the patterns allow a perfect reconstruction of the original object in the case of two-dimensional (2-D) noise-free data.

In the design of a coded aperture camera, the first challenge is to pick the pattern family that best suites the application and, within it, the pattern of the right size. A second and more serious challenge is that most literature is concerned with far-field problems, where the source is so far from the detector that all rays from the same point source can be considered parallel. However, in applications such as nuclear medicine, it is key to maximize efficiency, which leads to moving the detector as close as possible to the source, often until this far-field condition no longer holds. We face, then, a near-field problem: theoretical investigation, simulation, and experiments show that a straightforward application of the methods that in far field guarantee ideal imaging produces near-field images with serious artifacts.

In this paper, we present a coded aperture mask capable of high-resolution planar imaging with a commercial Anger camera over a field of view (FoV) of 9 × 9 cm. After providing the basics of coded aperture theory, we describe characteristics of the mask such as size, thickness, material, fabrication technology, pattern, and symmetry, showing how SNR and artifact reduction considerations enter the design. The results of some preliminary simulations are then compared to experimental data. Exploratory *in vivo* studies of ^{99m}Tc-labeled compounds in mice are also included. The paper closes with experimental verification of the design resolution and a discussion of the cases in which coded apertures fulfill their potential for high-resolution high-SNR images.

II. Coded Aperture Imaging

When the use of refraction or reflection optics is not practical due to the energy of the photons involved, the most straightforward way of obtaining an image is a pinhole camera. If the pinhole is infinitely small, the object is imaged with perfect resolution, but the transmitted power is also infinitely small, which produces noisy images. One can think of using a larger pinhole: while this allows more signal through the aperture, it also degrades resolution. The fundamental idea of coded apertures is to increase signal throughput by opening multiple small pinholes—thus retaining resolution—rather than a large one. Since each pinhole of the aperture generates an image of the object on the detector (see Fig. 1) and all projections overlap, the detector does not produce an image directly. However, from the overlapped copies and knowledge of the pinhole locations one can recover a clear image of the object. The restoration process is fast and does not introduce artifacts if certain arrangements of the pinholes (called coded apertures or masks) are used. An alternative way of looking at this same process is to think that each point in the source casts a shadow of the mask on the detector. Each point source is, thus, not revealed by a single bright spot, but rather by a pattern of spots. In this sense, we say that the mask is encoding the signal from the source. Due to encoding, the data are not immediately interpretable. To understand how an image is decoded we first need to describe the physical process of projection through the mask in mathematical terms.

Manuscript received May 2, 2001; revised July 20, 2001. This work was supported by the Office of National Drug Control Policy under Contract DAAD07-98-C-0117 and by the Federal Aviation Administration under Grant 93-G-053.

R. Accorsi and R. C. Lanza are with the Nuclear Engineering Department, Massachusetts Institute of Technology, Cambridge, MA 02139 USA.

F. Gasparini is with the Dipartimento di Ingegneria Nucleare, Politecnico di Milano, Milano, Italy.

Publisher Item Identifier S 0018-9499(01)10855-5.

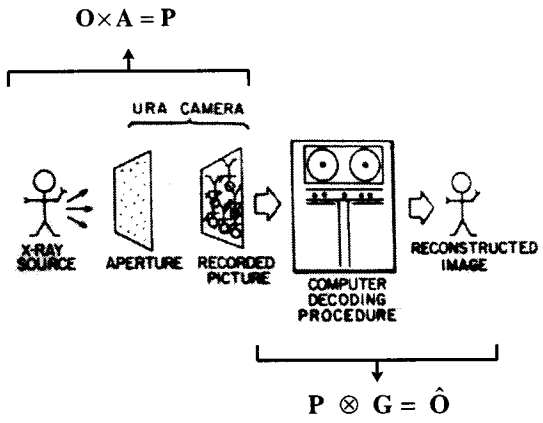

Fig. 1. Coded aperture camera concept: adapted from [9].

The data recorded by the detector $\boldsymbol{P}$ can be shown with elementary geometry to be related to the correlation ($\times$) of the source distribution (or object $\boldsymbol{O}$) with the mask pattern ($\boldsymbol{A}$) (see also Fig. 1)

$$\boldsymbol{P} = \boldsymbol{O} \times \boldsymbol{A}. \tag{2.1}$$

This first step is a purely physical process. Its endpoint $\boldsymbol{P}$ is the encoded image. The reconstructed image $\hat{\boldsymbol{O}}$ is then obtained from $\boldsymbol{P}$ by correlation with a decoding 2-D array $\boldsymbol{G}$

$$\hat{\boldsymbol{O}} = \boldsymbol{P} \otimes \boldsymbol{G} = (\boldsymbol{O} \times \boldsymbol{A}) \otimes \boldsymbol{G} = \boldsymbol{O} * (\boldsymbol{A} \otimes \boldsymbol{G}) \tag{2.2}$$

where $*$ indicates convolution and $\otimes$ correlation with periodic boundary conditions. This second step is called decoding and can be carried out with a digital computer. Equation (2.2) indicates that the reconstruction of the object is given, as in all linear systems, by the convolution of the original object with a kernel, the point spread function (PSF) of the system, where

$$\text{PSF} = \boldsymbol{A} \otimes \boldsymbol{G}. \tag{2.3}$$

The choice of the pair ($\boldsymbol{A}$, $\boldsymbol{G}$) is critical. In fact if

$$\boldsymbol{A} \otimes \boldsymbol{G} = \boldsymbol{\delta} \tag{2.4}$$

from (2.2) we see that $\hat{\boldsymbol{O}} = \boldsymbol{O} * \boldsymbol{\delta} = \boldsymbol{O}$. In this case, the pair ($\boldsymbol{A}$, $\boldsymbol{G}$) is said to have perfect imaging properties. Fortunately, both $\boldsymbol{A}$ and $\boldsymbol{G}$ may be chosen by the designer. Even better, pairs satisfying (2.4) are found in the literature; two particular cases are those of the uniformly redundant arrays (URAs, [9]), and of the m-sequences [10], for which $\boldsymbol{G} = \boldsymbol{A}$.

The mask array $\boldsymbol{A}$ is a "binary array" because its elements can take only one of two different values, 0 or 1, representing, respectively, totally opaque or transparent positions (mask pixels). In practice, in γ-ray imaging no mask is completely opaque but it turns out that partial transparency of the mask only affects the SNR of the system, not its resolution, and does not generate artifacts [16], [17].

Of course, within any family with perfect imaging properties, all patterns have perfect properties. So far, all patterns and families are completely equivalent. To explain the choice of the pattern we used, we first need to introduce some more design considerations.

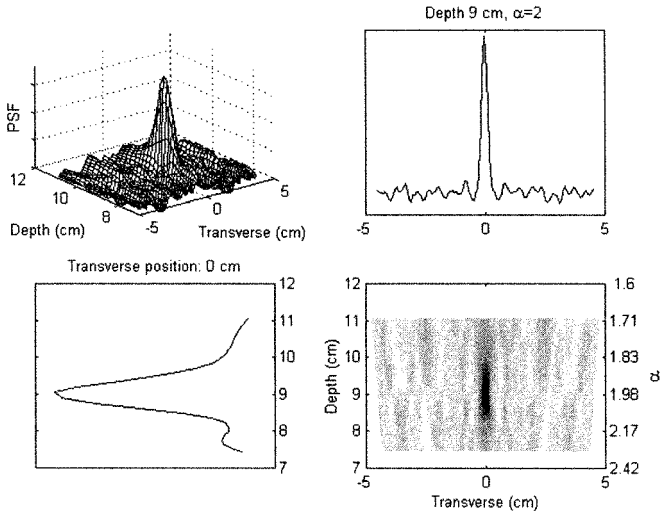

Fig. 2. Experimental 3-D PSF. The image at the bottom right is a color-coded top view of the 3-D plot at the top left. At the other corners are two sections through the peak. The FWHM in the transverse direction is about 3 mm, due to 1.67-mm system resolution plus about 1 mm of width of the point source used. The FWHM in depth is very close to 1 cm, a factor of five worse than the transverse FWHM (the point source was fairly flat, so the FWHM must be compared to 1.67 mm, not 3 mm). Note that the field of view is a function of depth. Total number of counts 1.6×10^6 obtained in 735 s from ^{99m}Tc. Depth measured from the mask (mask-to-object distance).

Before closing this section we wish to point out that the theory so far developed holds for planar objects only. In three-dimensional (3-D) cases, the size of the projection of the mask on the detector depends on the depth of the point source casting the shadow. There is then, associated with each depth, a different size of the decoding pattern $\boldsymbol{G}$. Decoding must be carried out for a given size and, thus, a given depth. All sources at this depth are decoded correctly, but all others, outside this focal plane, are not, and contribute artifacts to the image, unless 3-D techniques are used. These methods are outside the scope of this paper which is limited to planar imaging. However, this does not mean that our findings are limited to academic cases such as point and line sources. In fact, the important case of near-planar objects, i.e., as those objects whose thickness is no larger than the depth of focus of the instrument, can also be considered a 2-D application. In our case, the depth of focus was experimentally determined to be about 1 cm fullwidth at half-maximum (FWHM) (Fig. 2).

III. Mask Specifications

In designing the mask we optimized several features and parameters: pattern family, particular pattern within the family, pattern symmetry and shift, hole size, mask thickness, material and fabrication technology, magnification, and object-to-detector distance. In the following we give a brief explanation of each choice.

A. Material and Fabrication Technique

The best material from which to fabricate the mask is, not surprisingly, the one having minimum thickness for a given attenuation. From the theory of γ–ray attenuation, this is the material with the maximum product $\mu \cdot \rho$, with μ attenuation coefficient at, e.g., 140 keV and ρ density of the material. The best

material is uranium (48.97 cm^{-1}), followed by platinum (38.4 cm^{-1}), gold (35.9 cm^{-1}), tungsten (30.5 cm^{-1}), and lead (22.96 cm^{-1}). The choice is dictated by practicality, availability, cost, and fabrication technology. We picked tungsten and, since it is very hard to machine, we chose to photo-etch the pattern.

If all opaque positions have at least one horizontal or vertical neighbor, the pattern structure is said to be self-supporting. Non-self-supporting masks can be built only if some structure, for instance an aluminum back plane, can be inserted to ensure structural integrity. The drawback of photo-etching is that non-self-supporting arrays are very difficult to make (if at all) because the mask is built from very thin layers (which will be stacked later) each of which has the shape of the mask.

B. Mask Pattern Family

All the pattern families of [9]–[15] have ideal imaging properties and are, thus, equivalent from the point of view of image reconstruction in the case of infinitely good statistics. However, not all of them present the same SNR. For instance, simulation indicates and theory proves [16], [12] that the arrays suggested in [12]–[14] have lower SNR than URAs [9], the modified URAs (MURAs, [11]), and no-two-holes-touching (NTHT) (M)URAs [15]. [(M)URAs indicates both MURAs and URAs]. Since (M)URAs are not self-supporting, we chose NTHT (M)URAs. These patterns are derived from (M)URAs by inserting between all rows and columns some constant number of opaque rows and columns. Since in [16] it is proved that the SNR of NTHT (M)URA patterns is an increasing function of the open fraction, we analyzed only NTHT patterns obtained with the insertion of one row and one column. For this reason, the NTHT patterns we considered are twice the size of a (M)URA pattern.

C. Mask Symmetry

As anticipated in the Introduction, when coded apertures are used in a near-field geometry, artifacts arise. A detailed discussion of this problem is outside the scope of this paper and can be found elsewhere [17]. Briefly, the problem arises from the fact that in near-field geometry the projection of the mask on the detector is not the mask itself, but the mask modulated by the cube of the cosine of the incidence angle. Consequently, (2.1) does not hold rigorously because nonlinearities are introduced, and the linear reconstruction process presented does not lead to an exact reconstruction of the object. Here it is important to mention the result that, to eliminate such artifacts, one can divide the exposure time in two and take two pictures, one with a coded aperture, and a second with its negative, i.e., an aperture with opaque and transparent elements interchanged (antimask), and add them [17]. Furthermore, if the mask pattern is antisymmetric, e.g., about its center, one can build one mask only and use it to take both pictures. In fact, since the antimask can be obtained with a rotation of the mask, one can take the second picture after rotating the mask. This greatly simplifies moving mechanisms and reduces cost [18]. An example of the whole procedure can be found in Fig. 3. The limitation of this approach is that it reduces the number of available patterns.

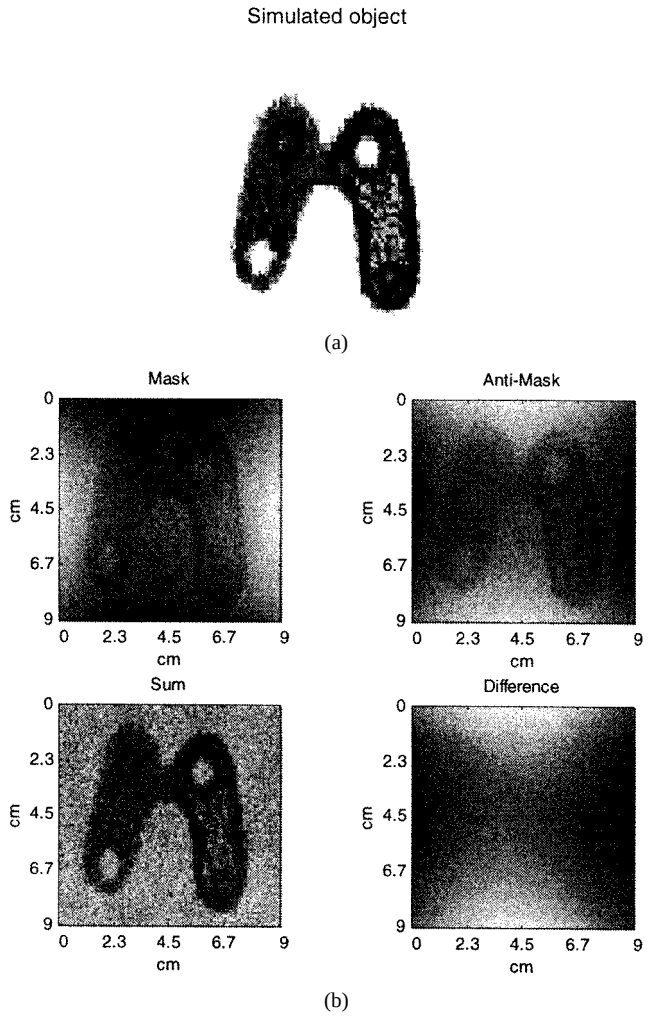

Fig. 3. Example of near-field artifact elimination. Simulation of a thyroid study. (a) Simulated object. (b) Reconstructions of the simulated object. Top left: reconstructed image when the mask was used. Top right: reconstructed image when the antimask was used. Bottom left: the previous two pictures are added. The object is reinforced while artifacts cancel out. Bottom right: if the reconstructed images are subtracted the opposite happens, i.e., the object cancels while artifacts are reinforced.

The mask/antimask technique was suggested and applied before (see [19]) to reduce the effects of nonuniformites in background count rates. We believe we are the first to suggest that the same technique can also be useful in the reduction of near-field artifacts.

D. Mask Pattern

Since we were interested in designing an aperture for use with an existing detector, its dimensions were chosen starting from those of the detector, a Siemens E-Cam gamma camera, with a 53.3 cm $\times$ 38.7 cm active area and 3.7-mm intrinsic resolution. The number of active pixels was chosen by looking at proper sampling of the projection of the mask on the detector, which forced the mask pattern not to exceed 80 $\times$ 80 pixels. An NTHT (M)URA pattern of this size does not exist. The largest available pattern is 74 $\times$ 74, but it is not antisymmetric. We chose the next pattern, a 62 $\times$ 62 NTHT MURA. The pattern was mosaicked, i.e., repeated four times except for a row and a column

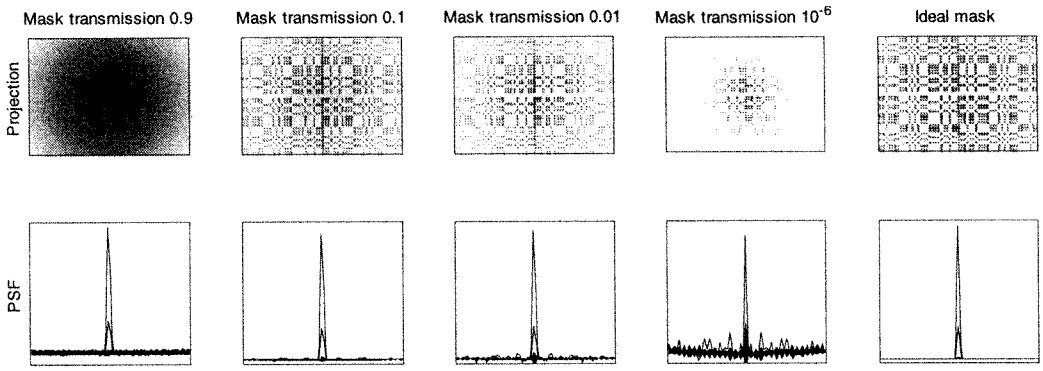

Fig. 4. Simulation of the projection of a point source (^{99m}Tc) and reconstruction for increasing mask thickness (decreasing transmission), left to right. A tungsten mask was assumed. Ideally, the projection should be a replica of the mask pattern. As thickness increases, rays that should pass are blocked. Therefore, in (2.1) $\boldsymbol{O}$ is not correlated with $\boldsymbol{A}$ but with a distortion of $\boldsymbol{A}$ dependent on source position. Successive decoding (correlation with $\boldsymbol{G}$) cannot generate a $\boldsymbol{\delta}$, giving rise to artifacts that add to near-field artifacts. To show the former artifacts, in each figure of the lower row all columns of the reconstructed image are shown (one for each trace). The ideal mask is one that is infinitely thin and yet perfectly opaque.

to avoid aliasing [9], to maximize detector usage. This design gives maximum resolution for a given field of view (see below). The open fraction of this pattern is 12.5%. This value may seem low, but for non-point-like objects, such as the thyroid of our simulations, the SNR of this family is not a strong function of the open fraction for open fractions above a few percent [16].

E. Mask Physical Dimensions

To determine mask dimensions we had to choose a field of view. Since previous coded aperture work of this group and many literature cases focused on thyroid imaging, we chose a field of 9 cm $\times$ 9 cm. This choice, given the portion of the detector actually used (124 $\times$ 124 pixels, so that the projection of each mask pixel is sampled twice), leads to a magnification of 3.305, and a hole size of 0.11 cm. On this basis, the geometric resolution of the coded aperture camera was calculated to be 1.45 mm, which becomes 1.67 mm when the intrinsic resolution of the detector is also accounted for.

F. Mask Thickness and Object-to-Detector Distance

The mask thickness was chosen from a compromise between high SNR and artifacts. In fact, if the mask is made too thin, it will be too transparent, and the signal will be hidden in false counts. On the other hand, if the mask is made too thick, rays that should pass are blocked. For example, photons directed to an open position from an off-axis angle could be blocked by the outstanding edge of adjacent mask elements. Of course, the effect depends on the energy of the photons, the extension of the object, and the material of which the mask is made, but in any case, the photon flux is at least partially collimated and artifacts result (Fig. 4). To guide our choice we defined a figure of merit based on the reconstruction of a point source. The figure of merit was defined empirically to be the standard deviation from the reconstructed peak of the activity in the reconstructed image. First, we verified that this definition can handle consistently statistical noise and artifacts, which have, in principle and in practice, very different effects on the image; then we evaluated it by computer simulation for different mask thicknesses and object-to-detector distances. The result is given in Fig. 5. On its basis, we chose a thickness of 1.5 mm and an object-to-detector distance of 40 cm. In tungsten at 140 keV, 1.5 mm provide 99% attenuation. From the magnification coefficient one can calculate that the object-to-mask distance is 9.3 cm and the mask-to-detector distance is 30.7 cm. From Fig. 5, we see that a thinner mask at 30 cm would give slightly better performance, but we wanted to build a mask that would also be useful in trials with higher energy isotopes.

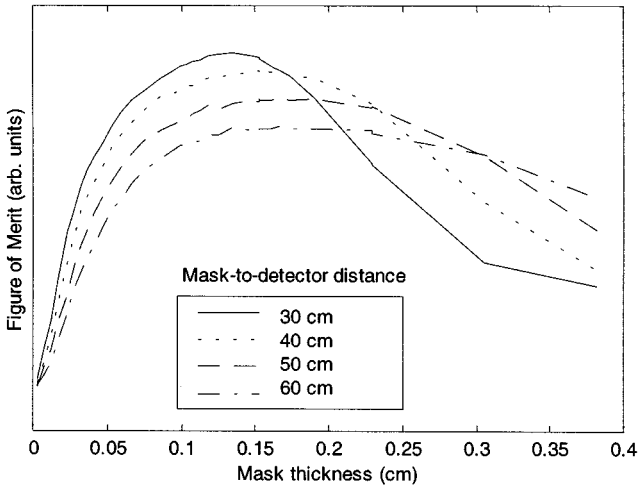

Fig. 5. Figure of merit of the reconstruction of a point source (^{99m}Tc) as a function of mask thickness (for tungsten), for different values of the object-to-detector distance. For any distance, at the left of the graph the FoM increases because the increasing mask thickness makes the mask more opaque with little collimation (see Fig. 4). As thickness increases, collimation effects become more severe while the incremental reduction in transparency decreases. Eventually, collimation prevails and sinks the FoM, generating a maximum. At high object-to-detector distance, the maximum occurs for higher mask thickness because incidence angles, and thus collimation, are lower. However, due to poorer efficiency, the maximum FoM is not as high as for lower distances.

All mask characteristics discussed above are summarized in Table I.

IV. Experimental Results

A. Testing the System

The first experiments compared the performance of the system to that expected from the design. At the top left of

TABLE I
SUMMARY OF THE PROPERTIES OF THE FABRICATED MASK

Mask pattern		NTHT MURA 62×62
Open fraction		12.5%
Mosaicked		yes
Self-supporting		yes
Mask pixel size		1.11 mm
Resolution (at FoV = 9 cm)	geometric	1.45 mm
	system	1.67 mm
Mask symmetry		anti-symmetric about center
Material		Tungsten
Fabrication technology		Photo-etching
Thickness		1.5 mm
Attenuation at 140 keV		99%

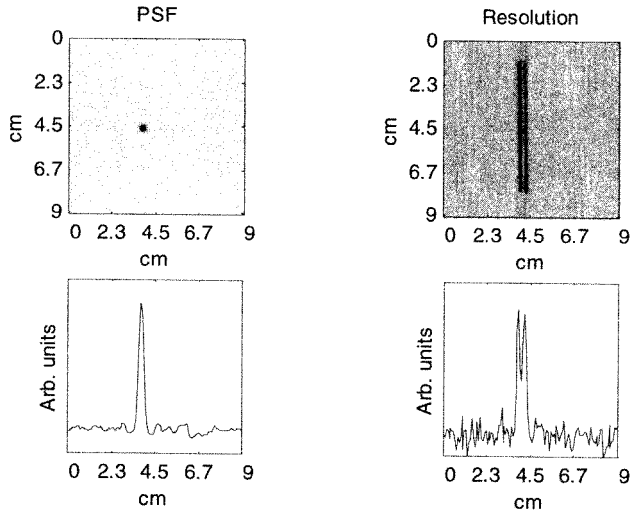

Fig. 6. PSF and resolution test with two line sources with a center-to-center distance of 3.1 mm.

Fig. 6 is a sample PSF. The horizontal section through the peak is below the image. Note that due to the finite size of the point source used, its image spreads over a few pixels. The response of the system is ideal in the sense of Section II.

To test resolution and FoV we built a test source made of three identical capillaries. According to the specifications, each tube was 75-mm long, the internal diameter was 1.15 ± 0.05 mm with a wall thickness of 0.2 ± 0.02 mm. Two tubes were injected with 150 μCi of ^{99m}Tc each, while the third was left empty and used as a spacer between the other two. Consequently, the inner-edge-to-inner-edge distance was 1.95 ± 0.094 mm, while the center-to-center distance was 3.1 ± 0.128 mm. Two images were taken, each for a total of 2×10^6 counts, each requiring an exposure time of 85 s, which indicates a sensitivity of $\sim$9400 cpm/μCi. At the top right of Fig. 6 is the result of the sum of the two images. At the bottom right, a horizontal section is shown.

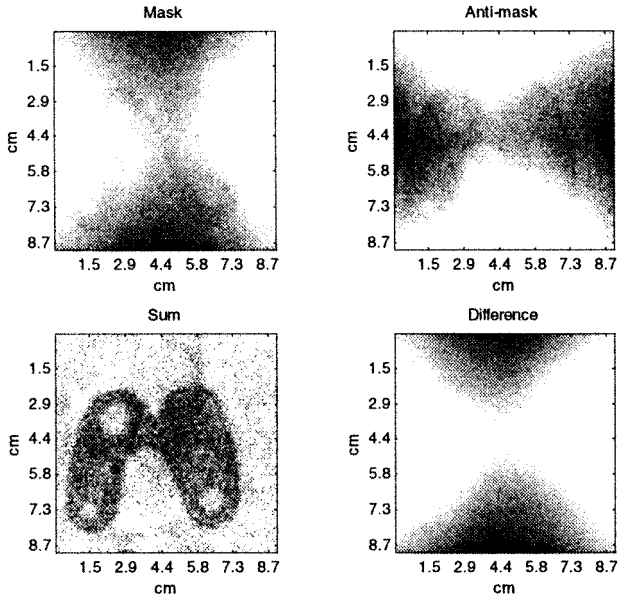

Fig. 7. Experimental result: thyroid phantom. Compare with the simulation of Fig. 3 (where cold and hot spots are different in number and location).

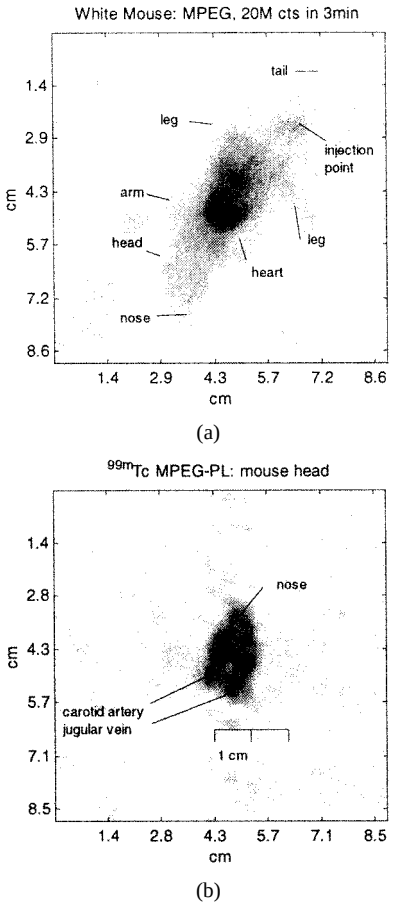

Fig. 8. Images of a mouse after injection of a radioactive tracer: blood pool agent. (a) Body scan of a white mouse. Total exposure time 6 min 30 s. Total number of counts 40×10^6. Activity injected 1.5 mCi. (b) Same situation except the body below the neck was shielded with a lead sheet. Details of the head are now clearly visible. Exposure time for the mask picture: 277 s. Exposure time for the antimask picture 279 s. In both pictures the total number of counts was 5×10^6 per exposure.

Since our system was designed for 1.67-mm resolution, the cap-

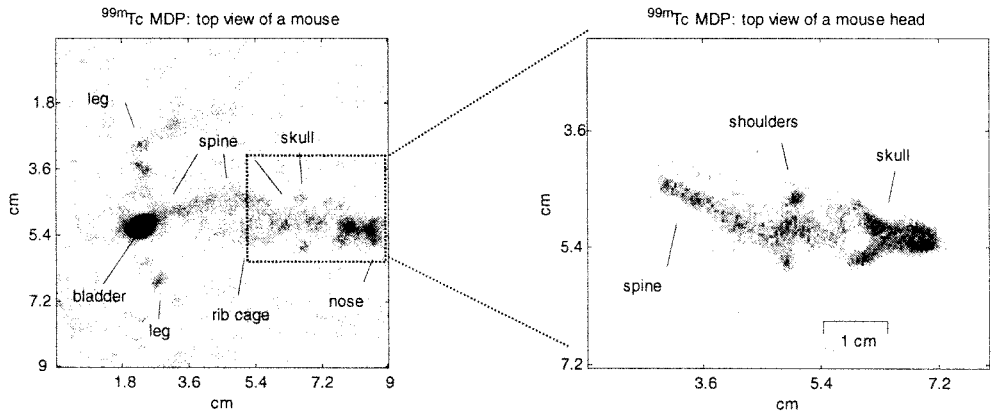

(a) (b)

Fig. 9. Images of a mouse after injection of a radioactive tracer: bone agent. (a) Whole body scan of ^{99m}Tc-MDP in a mouse. Top view. Exposure time for the mask picture: 490 s. Exposure time for the antimask picture 495 s. In both pictures the total number of counts was 4×10^6. Injected activity: 100 μCi. Most of it ends up in the bladder. (b) After shielding, the mouse from the flanks down, the SNR is improved. Exposure time for the mask picture: 739 s. Exposure time for the antimask picture 754 s. In both pictures the total number of counts was 2×10^6.

illaries are resolved well (note that if the resolution of a system is defined as the FWHM of the PSF and the PSF is Gaussian, a 7% dip between two sources is sufficient to resolve two points).

B. Artifact Reduction

Artifact reduction was tested with a 2-D phantom. This is a Picker thyroid phantom where only the bottom was filled with 350 μCi of ^{99m}Tc. The expected activity distribution is a constant level. There is no hot or cold lobe as would be had the phantom been completely filled. There are only three round cold spots with no activity. Deviations from this ideal situation are due to variations in depth of the radioactive solution caused by a slight tilt of the phantom holder. Two 20×10^6 counts images were taken each in about 500 s. The results for mask and antimask are shown at the top of Fig. 7. Just as in the simulations of Fig. 3, the sum of the images reduces the artifacts, while taking the difference eliminates the object. The injection channel is recognizable at the top of the right lobe.

C. A Real Case

The coded aperture camera was next tested in a real study of the distribution of a labeled compound in a mouse. In the first case, the mouse was injected with a blood pool agent, MPEG-PL, labeled with ^{99m}Tc. In Fig. 8(a), the shape of the body is clearly recognizable. Most of the activity is concentrated in the trunk. Activity outside the body is also visible, but can be discriminated by resetting the lower threshold of the color scale. Resolution is high as compared to collimator scans, but the SNR is poor at dim points. This is expected from the SNR theory of coded apertures, for which advantages are highest, if present at all, for points where the highest fraction of the activity is concentrated [20], [16].

Since we were interested in the head only, the rest of the mouse was shielded with a lead sheet. This shielding aims at increasing the mentioned fraction of the total activity at points of the head by decreasing the total activity in the object. Two images (mask and antimask) were taken, each for a total of 5×10^6 counts, in about 280 s. The sum image is in Fig. 8(b). The two main blood vessels in the neck (jugular vein and carotid artery) are clearly separated and other details of the vessels to and from the nose are also evident.

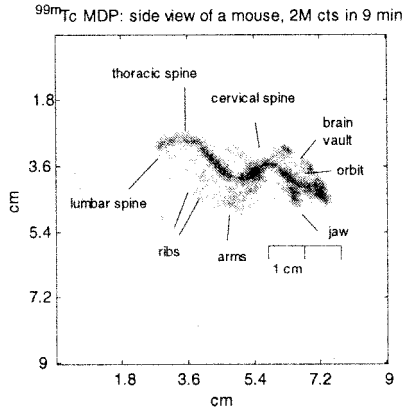

Fig. 10. Images of a mouse after injection of a radioactive tracer: bone agent. Side view. Activity injected: 300 μCi. Exposure time for the mask picture: 521 s. Exposure time for the antimask picture 531 s. In both pictures the total number of counts was 2×10^6.

The second study was a top view of a mouse injected with about 100 μCi of MDP, a bone agent, again labeled with ^{99m}Tc. Two sets of images, the second with the flanks from the bladder down shielded, were taken [Fig. 9(a) and (b)]. Again, the advantage of concentrating on the part of the body of interest is evident.

A side view of the mouse was also taken (Fig. 10). The spine is resolved in considerable detail and in the skull features: jaw, orbits, and brain vault are visible. The rib cage may be visible under the thoracic spine. A hint of the position of the front paws is also present.

V. Discussion

The mathematics of coded aperture imaging shows that apertures with perfect correlation properties provide ideal point spread functions, but this is true only in far-field cases. In near-field geometry (i.e., when rays coming from the same point source in the object cannot be considered parallel) many factors potentially cause deviation from ideality. Thick objects

cause artifacts because a one-view coded aperture camera can focus only on one object plane at a time: all other planes are out-of-focus and contribute artifacts to the image. In this paper, limited to planar studies, these artifacts were not a concern. An example is the case of small animals (typically mice) in molecular imaging.

A coded aperture mask for use with a pre-existing Anger camera was presented. Experimental results confirm that 1.67-mm resolution is achievable, to be compared to the 4–6 mm provided by current state-of-the-art pinhole and collimator systems. As compared to collimator images, the coded aperture camera offers a better resolution, higher SNR, but a smaller field of view, which is not a drawback in many cases, such as small animal imaging or exams of limited, thin, parts (e.g., hands) in humans. We should stress here that while high resolution is always achieved, the SNR advantage over collimator/pinhole systems is present for objects with activity spread over relatively few pixels (say, a tenth of the total. A more rigorous discussion is found in [16]). However, a considerable number of studies match this requirement. Examples are the head and bone scans seen above, whole body scans for tumor location or blood vessel studies aimed at detection of thrombi. Shielding parts of the source of little interest also helps to improve the SNR, an opportunity not provided by conventional technology. This is what we did in our mouse studies, where the activity in the bladder, which was of little interest, was shielded.

In the near future, we plan to explore if more aggressive designs involving different projection sampling strategies can improve resolution and if the results achieved for ^{99m}Tc photons can be extended to more energetic photons, such as those from ^{111}In (245 keV) and positron annihilation (511 keV).

ACKNOWLEDGMENT

The authors wish to thank R. Zimmerman of the Harvard Medical School and Brigham and Women's Hospital and A. Bogdanov and U. Mahmood of the Massachusetts General Hospital Center for Molecular Imaging Research for their help with the experimental work.

REFERENCES

[1] E. Caroli, J. B. Stephen, G. Di Cocco, L. Natalucci, and A. Spizzichino, "Coded aperture imaging in X- and Gamma-ray astronomy," *Space Sci. Rev.*, vol. 45, pp. 349–403, 1987.

[2] G. K. Skinner, "Imaging with coded-aperture masks," *Nucl. Instrum. Methods Phys. Res.*, vol. 221, pp. 33–40, 1984.

[3] A. Hammersley, T. Ponman, and G. Skinner, "Reconstruction of images from a coded-aperture box camera," *Nucl. Instrum. Methods Phys. Res.*, vol. A311, pp. 585–594, 1992.

[4] E. E. Fenimore, T. M. Cannon, D. B. van Hulsteyn, and P. Lee, "Uniformly redundant array imaging of laser driven compressions: Preliminary results," *Appl. Opt.*, vol. 18, pp. 945–947, 1979.

[5] Y. W. Chen, M. Yamanaka, N. Miyanaga, T. Yamanaka, S. Nakai, C. Yamanaka, and S. Tamura, "Three-dimensional reconstruction of laser-irradiated targets using URA coded aperture cameras," *Opt. Commun.*, vol. 71, pp. 249–255, 1989.

[6] K. F. Koral, J. E. Freitas, W. L. Rogers, and J. W. Keyes, "Thyroid scintigraphy with time-coded aperture," *J. Nucl. Med.*, vol. 20, pp. 345–349, 1979.

[7] W. L. Rogers, K. F. Koral, R. Mayans, P. F. Leonard, J. H. Thrall, T. J. Brady, and J. W. Keyes, Jr., "Coded-aperture imaging of the heart," *J. Nucl. Med.*, vol. 21, pp. 371–378, 1980.

[8] H. H. Barrett, "Fresnel zone plate imaging in nuclear medicine," *J. Nucl. Med.*, vol. 13, pp. 382–385, 1972.

[9] E. E. Fenimore and T. M. Cannon, "Coded aperture imaging with uniformly redundant arrays," *Appl. Opt.*, vol. 17, pp. 337–347, 1978.

[10] E. E. Fenimore, "Large symmetric π transformations for Hadamard transforms," *Appl. Opt.*, vol. 22, pp. 826–829, 1983.

[11] S. R. Gottesman and E. E. Fenimore, "New family of binary arrays for coded aperture imaging," *Appl. Opt.*, vol. 28, pp. 4344–4352, 1989.

[12] S. R. Gottesman and E. J. Schneid, "PNP—A new class of coded aperture arrays," *IEEE Trans. Nucl. Sci.*, vol. NS-33, pp. 745–749, 1986.

[13] K. Byard, "On self-supporting coded aperture arrays," *Nucl. Instrum. Methods Phys. Res.*, vol. A322, pp. 97–100, 1992.

[14] ——, "Synthesis of binary arrays with perfect correlation properties—Coded aperture imaging," *Nucl. Instrum. Methods Phys. Res.*, vol. A336, pp. 262–268, 1993.

[15] E. E. Fenimore and T. M. Cannon, "Uniformly redundant arrays: Digital reconstruction methods," *Appl. Opt.*, vol. 20, pp. 1858–1864, 1981.

[16] R. Accorsi, F. Gasparini, and R. C. Lanza, "Optimal coded aperture patterns for improved SNR in nuclear medicine imaging," *Nucl. Instrum. Methods Phys. Res.*, vol. A474, pp. 273–284, 2001.

[17] R. Accorsi and R. C. Lanza, "Near-field artifact reduction in coded aperture imaging," *Appl. Opt.*, vol. 40, no. 26, pp. 4697–4705, 2001.

[18] U. B. Jayanthi and J. Braga, "Physical implementation of an antimask in URA based coded mask systems," *Nucl. Instrum. Methods in Phys. Res.*, vol. A310, pp. 685–689, 1991.

[19] M. L. McConnell, D. J. Forrest, E. L. Chupp, and P. P. Dunphy, "A coded aperture gamma ray telescope," *IEEE Trans. Nucl. Sci.*, vol. NS-29, pp. 155–159, 1982.

[20] E. E. Fenimore, "Coded aperture imaging: Predicted performance of uniformly redundant arrays," *Appl. Opt.*, vol. 17, no. 22, pp. 3562–3570, 1978.